Physics-Informed Battery Aging Model under Marine Transport Swaying Conditions

Yingbing Luo[1] *Student member, IEEE*, Laiqiang Kong[1] *Student member, IEEE*, Peng Wu[2], Sidun Fang*[1] *Senior member, IEEE,* Tao Niu[1] *Senior member, IEEE*, Guanhong Chen[1] *member, IEEE*, Ruijin Liao[1] *IEEE*

***Abstract*—Large-scale lithium-ion battery applications significantly promote marine transport decarbonization. However, inevitable marine transport swaying conditions markedly deteriorate the health of batteries. There are no quantitative methods to elucidate unique degradation behaviors and their unknown interdependencies. In this context, this paper proposes a physics-informed battery aging model (PIBM). First, the dominant aging patterns of batteries affected by the external mechanical stress are revealed through a laboratory-scale experimental system with standard marine transport swaying conditions. Then, a universal pseudo-two-dimensional (P2D) electrochemical model combining coupled degradation mechanisms is introduced to quantify the particle-level state degradation. Subsequently, a general data-driven strategy that respects physical causality is embedded into the modified P2D model. This strategy can approximate the finite-order partial differential equations and efficiently resolve the full-life Li^+ diffusion dynamics. Compared with the conventional hybrid data-driven model, the proposed method quantifies the health degradation of batteries from the particle to the cell level and demonstrates more accurate and faster performance.**

***Index Terms*—Marine transport swaying conditions, Lithium-ion battery (LiB), Coupled degradation mechanisms, Physics-informed battery aging model (PIBM).**

NOMENCLATURE

PIBM, Physics-informed battery model.
OLHM, Open-loop hybrid model.
BPLM, Back-propagation learning machine.
$i = n, p$, Description of negative (n) and positive (p).
$c_{s,i}$, Lithium-ion concentration of electrode (mol/m^3).
c_e, Lithium-ion concentration of electrolyte (mol/m^3).
$D_{s,i}^{eff}$, Diffusion coefficient of electrode (m^2/s).
D_e^{eff}, Diffusion coefficient of electrolyte (m^2/s).
r, Radial coordinate (m);
R, Particle radius (m).
x, Spatial coordinate (m);
L, Length of Cell (m).
σ^{eff}, Electric conductivity of electrode (S/m).
κ^{eff}, Electric conductivity of electrolyte phase (S/m).
$\phi_{s,i}$, Electric potential of electrode (V).
ϕ_e, Electric potential of electrolyte phase (V).
$\epsilon_{s,i}$, Volume fraction of electrode (mol/m$^3\cdot$ s^{-1}).
ϵ_e, Volume fraction of the electrolyte (mol/m$^3\cdot$ s^{-1}).
t^+, Transference number of lithium-ion.
F, Faraday's constant (96485.3 C/mol).
R_g, Molar gas constant (8.314 J/(mol$\cdot$ K)).
T, Kelvin temperature (K).
j Interfacial current density of electrode (A/m^2)
j_{sei} Interfacial current density of SEI layer (A/m^2)
i_0, Exchange current density (A/m^2).
$a_{s,i}$, Specific surface area of electrode (m^2), $s = n, p$.
I_{app}, Applied current (A).
$\eta_{s,i}$, Overpotential of electrode (V).
c_s^{max}, Maximum concentration of electrode (mol/m^3).
c_s^{surf}, Surface concentration of electrode (mol/m^3).

I. INTRODUCTION

A. Background and motivation

THE global marine lithium-ion battery (LiB) market is forecast to expand at 17.1% per year by 2030, promoting sustainable development in electrified marine transport systems [1], [2]. However, uncertain marine transport swaying conditions easily exacerbate the coupled mechanical-electrochemical processes of LiBs, resulting in irreversible health degradation and even thermal runaway [3]. As a result, LiB's life and safety have emerged as the primary concerns in harsh marine applications.

Conventional destructive tests or qualitative models make it hard to capture particle-level degradation efficiently, and identifying unique degradation mechanisms directly presents a significant challenge [4]. Although interpretable insights into degradation patterns are critical for observing state-of-health (SOH) variations, they significantly increase the order and solution complexity of electrochemical models [5]. Therefore, there is a motivation to establish a non-destructive and efficient battery aging model suitable for harsh marine applications.

B. Literature survey

Affected by unpredictable wind, waves, and ocean currents, marine transport systems such as ferry, dynamic position platform, tugboat, and barge, etc., are always in motion with six degrees of freedom, which inevitably exposes the onboard LiBs to swaying effects, characterized by high-amplitude and low-frequency vibrations, about the oscillation frequency of 0.1-0.2 Hz [6]. As for LiBs, external mechanical stress is an important source of the internal stress field, easily accelerating their electrochemical reaction and even damaging the electrode material structure [7]. For example, mechanical stress damages

[1]The School of Electrical Engineering, Chongqing University, Chongqing, China, 400044.
[2]University College London, Department of Mechanical Engineering, London, United Kingdom, WC1E 6BT.
Corresponding author: Sidun Fang. Email: fangston@cqu.edu.cn
This study work is supported by the Smart Grid-National Science and Technology Major Project, Project No. 2025ZD0805401, the National Natural Science Foundation of China, Project No. 5257070416, and the China Scholarship Council Project, Project No. 202506050093.

electrode particles and further thickens the solid electrolyte interphase (SEI) layer, which is always regarded as a dominant degradation factor [8]. Then, a series of side reactions caused by coupled mechanical-electrochemical processes are formulated in [9], including loss of lithium-ion inventory (LLI) and porosity reduction. Moreover, tests with different vibration frequencies (20 Hz, 50 Hz, and 75 Hz) all show that the negative electrode graphite particles undergo cracking and stripping, leading to the increase of ohmic resistance and the loss of active material (LAM) [10]. Based on material characterization techniques at the microscopic scale, the quantitative analysis concluded that LLI and LAM are the dominant degradation mechanisms under vibration [11]. Furthermore, reference [12] shows that vibration amplitude has a greater impact on the aging of LiBs in the Z-axis direction, while vibration frequency has a greater impact on aging in the X-axis and Y-axis directions. Similarly, as a special vibration condition, the mechanical stress generated by swaying may also significantly change the internal operating characteristics of LiBs, thereby deteriorating their health and performance. Nevertheless, existing studies focus more on the operating conditions of terrestrial electric vehicles and rarely consider the marine transport swaying conditions. As a result, the impact of marine transport swaying conditions on LIBs remains poorly understood, and there is still a lack of abundant experimental data and quantitative approaches to characterize the impact of swaying effects, which are essential for accurate SOH estimation under long-term application.

The available experimental data provide a foundation for accurate SOH diagnosis, and numerous studies have been conducted. Generally, the internal resistance variations of LiBs are used to assess their health level in most commercial applications [13]. Similarly, periodic full charge-discharge capacity testing [14] and open-circuit voltage (OCV) testing [15] can effectively correct the health level, but are unsuitable for frequent discharging conditions such as electrified marine transport propulsion. Moreover, the relaxation voltage [16], terminal voltage decay rate [17], and discharging/charging time-ratio features [18] are also considered as degradation features. For example, the peak distribution features of the incremental capacity (IC) are utilized to capture the coupled relationship between charging capacity and voltage decay [19]. Additionally, frequency-domain health indicators are integrated to achieve excellent estimation performance, but the accurate decomposition of the frequency range poses a high requirement on a profound understanding of physical characteristics within LiBs [20]. Therefore, combining the author's existing knowledge, three primary challenges are summarized, including: 1) the evolution of LiB performance under swaying conditions remains underexplored, 2) without a high-fidelity mechanistic foundation, the established models cannot be assured to adhere to the governing physics [21], and 3) the absence of aging features with embedded physical principle makes it hard to characterize the LiB aging behaviors [22]. In this background, a comprehensive and accurate formulation of the electrochemical/physical behaviors is a prerequisite for quantifying the health degradation of LiBs.

The conventional pseudo-two-dimensional model (P2D) and single-particle model (SPM) can formulate the microscopic electrochemical behaviors of LiBs, such as partially reversible lithium-ion (Li^+) stripping/plating and SEI layer growth [23]. Although comprehensive insights can capture more underlying degradation behaviors, they improve the number and solution difficulty of interrelated partial differential equations (PDEs). To reduce complexity, existing equivalent circuit models can be utilized, but they lose an excellent opportunity to formulate electrochemical phenomena inside cells [24]. In contrast, data-driven methods provide a fresh perspective for establishing various nonlinear relationships observed from data directly. For example, gaussian process regression (GPR) [25], support vector regression (SVR) [26] and artificial neural networks (ANN) [27], etc. Nevertheless, these black-box models require numerous high-quality datasets and have long been criticized for their weak interpretability. But in an alternative view, many complex physical processes cannot be described directly by PDEs, but rather by a set of empirical laws [28]. These fail to be accurately formulated when data is scarce or in complex conditions, which sparks interest in hybrid models.

Conventional hybrid data-driven models tend to emphasize correlation features and always employ an open-loop framework to further improve accuracy and efficiency. For example, an ANN-combined electrochemical impedance spectroscopy (EIS) feature is investigated to estimate state-of-charge (SOC) [29]. Then, heterogeneous models using multi-layer learning mechanisms are investigated to maximize the aging model generalization [30]. These open-loop hybrid models (OLHM) have two characteristics: 1) the data-driven part only extracts partial physical features and does not provide any updated information to participate in the intermediate electrochemical solution process, and 2) they commonly oversimplify the physics that the degradation trends of LiBs should follow and can only ensure the accuracy of the interested parameters.

According to these issues, a physics-informed neural network (PINN) can simultaneously meet the model interpretability and generalizability, i.e., 1) the physical laws are embedded into the data-driven model in the form of residuals, which can limit the operating boundary of electrochemical states [31]; 2) Convolution kernels are trained to approximate finite-order PDEs, thereby significantly reducing the complexity of the model [32]. For example, a PINN model is investigated to generate numerous particle-level data and thereby evaluate the battery states [33]. Then, a grid-long short-term memory (Grid-LSTM) method is established to estimate Li^+ concentrations and potentials in electrodes [34]. However, most models avoid incorporating degradation mechanisms, as they still lack adaptability and struggle to balance complexity with accuracy. Especially, the assumption of a constant resistance makes it hard to accurately describe dynamic electrolyte concentration distribution [35]. This oversight may significantly undermine the model's performance as the LiB ages. Therefore, the above challenges impose higher requirements for embedding high-fidelity mechanistic insights into data-driven approaches, thereby improving the health assessment capability of LiBs under marine transport swaying conditions.

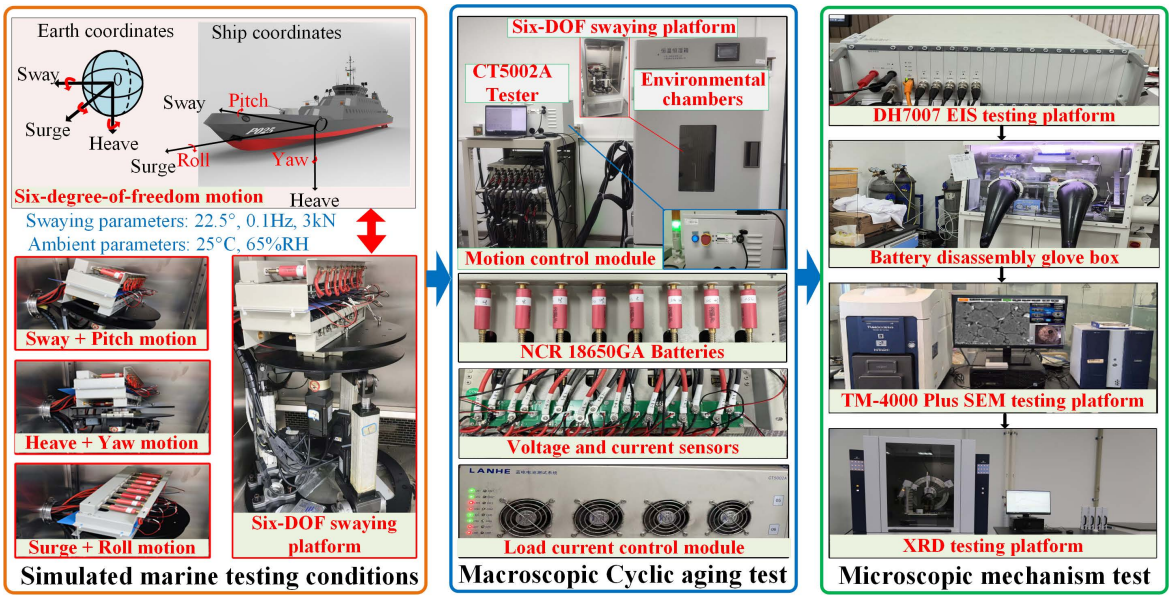

Fig. 1: LiB test platform under simulated marine environments.

C. Contribution

According to the above issues, this paper proposes a practical LiB aging model based on comprehensive physics principles. The main contributions are as follows:

1) This work carries out cyclic LiB tests under standard marine transport swaying conditions. Through macroscopic and microscopic analyses, the health degradation of LiBs affected by the mechanical stress can be quantified. Notably, the dominant aging factor is conductivity loss (CL) under swaying. As the number of cycles increases, the intensification of particle structure damage leads to LAM becoming the dominant degradation factor.
2) A physics-informed battery aging model framework (PIBM) that integrates coupled degradation mechanisms is proposed to highlight the potential of reconstructing electrochemical processes from the particle to the cell, thereby quantifying the health level of LiBs.
3) Based on particle-level degradation insights, the proposed PIBM can further evaluate cell-level aging efficiently, including terminal voltage decay, Li^+ dynamics, and SOH variations. Finally, the computational efficiency and accuracy of the proposed model are verified in swaying and different current conditions.

II. Aging Mechanism Analysis of Swaying Effects

A. Simulated marine experimental environments setup.

In electrified marine transport, essential tasks such as directional navigation, dynamic positioning, and docking inevitably cause swaying of the hull and battery compartment. To describe swaying effects, a laboratory-scale experimental system is established in Fig. 1, and the details are as follows:

1) Simulated marine environment settings: "Guidelines for Type Approval Testing of Electrical and Electronic Products in 2015" of the China Classification Society is used for primary reference [36]. The guideline specifies performance testing requirements for shipboard electrical equipment under swaying conditions, pointing out that swaying testing conditions with an inclination angle of 22.5°, an amplitude of 1 mm, a thrust of 3 kN, and a frequency of 0.1 Hz. Then, the ambient temperature is set to 25°C and the air humidity level is set to 65% RH, which represents a typical operating environment to avoid the influence of high humidity on the LiB performance.

2) Macroscopic cyclic aging test: Twenty-three identical NCR 18650GA LiBs are used to accomplish the cyclic aging test under swaying conditions. The parameters of LiBs are shown in Table. I, and the testing protocol is constant current and constant voltage (CCCV), the charge current rate is 0.5 C, and the discharge current rates range from 0.5 C to 3 C.

TABLE I: The NCR 18650GA LiB parameters.

Description	Value	Units
Cathode material	$Li(Ni_{0.80}Co_{0.15}Al_{0.05}O_2)$	[-]
Anode material	Graphite	[-]
Nominal capacity	3.35	[Ah]
Discharging cut-off voltage	2.4	[V]
Charging cut-off voltage	4.2	[V]
Cut-off current	0.1725	[A]
Experimental group	Swaying B1 - B12	[-]
Control group	Static B1 - B11	[-]

3) Microscopic mechanism test protocol: Firstly, EIS tests are performed every 10 charge-discharge cycles to monitor the battery impedance at 0% SOC. Upon retirement of the LiBs due to aging, they are disassembled in a glove box. Subsequently, the scanning electron microscope (SEM) is employed for observing the internal characteristics, such as SEI film thickness, pores, and particle cracks. Finally, the X-ray diffraction (XRD) is performed on the anode materials to observe the variation of their crystal structure.

B. Macroscopic effects of swaying on LiB aging

From a macroscopic perspective, the cyclic LiB aging results are shown in Fig. 2 [37]. Wherein, SOH is defined

as the remaining storable capacity, and it is commonly calculated by dividing the current test capacity C_{real} by the rated capacity C_0 when $SOH = \frac{C_{real}}{C_0}$ [38]. The black dotted line represents the end-of-life, i.e., SOH=0.8. It can be seen that the health degradation of LiBs is faster under swaying conditions, especially when the discharge current rate increases. However, under 0.5 C, only Swaying B2 ages more rapidly, and the health degradation trend of Swaying B1 and Swaying B3 is almost the same as that of Static B1 and Static B2. Additionally, the occasional upward trends observed in these health curves can be attributed to reversible structural alterations that occur during the discharge process, including the reorientation of electrode particles and the variations in pore dimensions. Coupled with the uniform distribution of the electrolyte, these factors may lead to a temporary increase in the available capacity [39], [40].

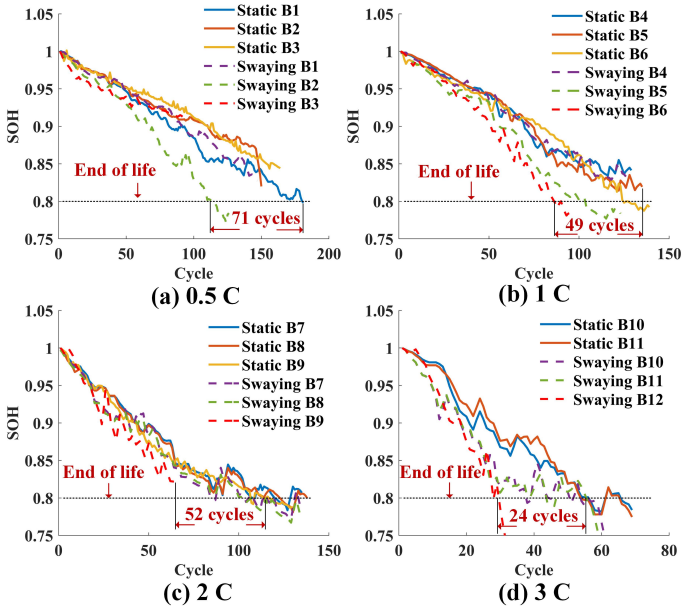

Fig. 2: Effect of swaying on cyclic LiB aging.

Then, the IC curve serves as a qualitative analysis tool for aging modes and can reflect the structural changes in electrode materials as well as the loss of active substances during the battery aging process, as shown in Fig. 3.

From Fig. 3, the IC curves feature three distinct peaks, and each peak varies in response to the increasing number of cycles. Under static conditions, from Fig. 3 (a1), (b1), (c1), and (d1), the increase in the discharge current rate leads to a narrowing of the voltage platform and a corresponding increase in Peak 3. This suggests that the phase transformation reactions of the materials significantly constrict the voltage plateau and enhance the rate of change of the stored capacity. The probable reason is that the high current rate degrades the mechanical properties of the materials, making the active particles more prone to cracking, which in turn results in a rapid capacity fade of the LiB. Under swaying conditions, as shown in Fig.3 (a1) and (a2), compared with the operational conditions at 0.5 C and static conditions, Peak 3 gradually shifts downward under swaying, while the trends of Peak 1 and

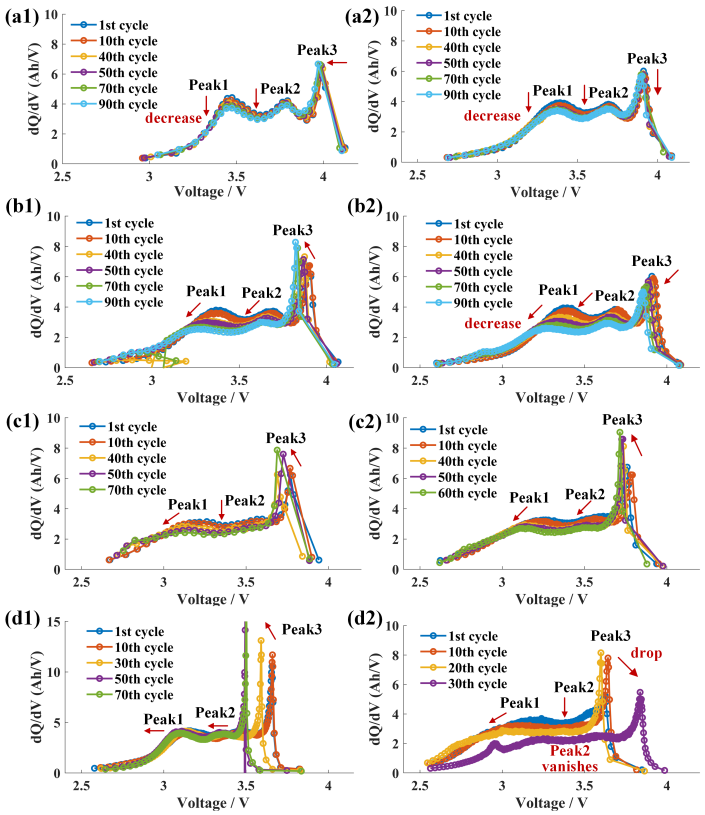

Fig. 3: Effect of swaying on IC curves: (a1) Static B3, 0.5 C; (a2) Swaying B3, 0.5 C; (b1) Static B6, 1 C; (b2) Swaying B6, 1 C; (c1) Static B9, 2 C; (c2) Swaying B9, 2 C; (d1) Static B11, 3 C; (d2) Swaying B12, 3 C.

Peak 2 remain consistent. This is because swaying stress tends to cause delamination between the active material and the current collector, rather than directly affecting the mechanical properties of the electrode materials as the high current rate does. Meanwhile, the stress generated by swaying causes slight cracking of the active material and the deposition of side reaction products, resulting in a reduction of the stored energy at the same voltage level. Then, from Fig. 3 (a2), (b2), (c2), (d2), the IC curve has a tendency to move toward low voltage, indicating that the increase in ohmic resistance exacerbates the CL of LiBs. Furthermore, compared to static conditions, Peak 3 predominantly exhibits a downward trend, indicating that LLI occurs under most conditions. Similarly, Peak 2 shifts toward the lower left and eventually disappears as the LiB ages, which can be attributed to the simultaneous occurrence of LLI and LAM. Especially, the gradual decrease and leftward shift of Peak 1 further illustrate the occurrence of LAM.

In conclusion, the stress generated by swaying can cause the connections between internal components of the LiB to become unstable. This instability is further exacerbated by the rapid expansion and contraction of electrode materials under high current rates. Under the combined effect of these two factors, the electrode materials are more likely to detach. The destruction of the internal structure of the battery accelerates, leading to a rapid reduction in the stored capacity.

However, it is difficult to precisely analyze the effects

of swaying based solely on IC curves due to the highly complex degradation mechanisms within the LiBs. Therefore, it is necessary to integrate more microscopic-scale mechanistic analysis approaches to quantify the swaying effects.

C. Microscopic effects of swaying on LiB aging

From a microscopic perspective, the EIS test, SEM test, and XRD test are accomplished, and the test results for Swaying B3, B6, B9, and B12 are shown as follows.

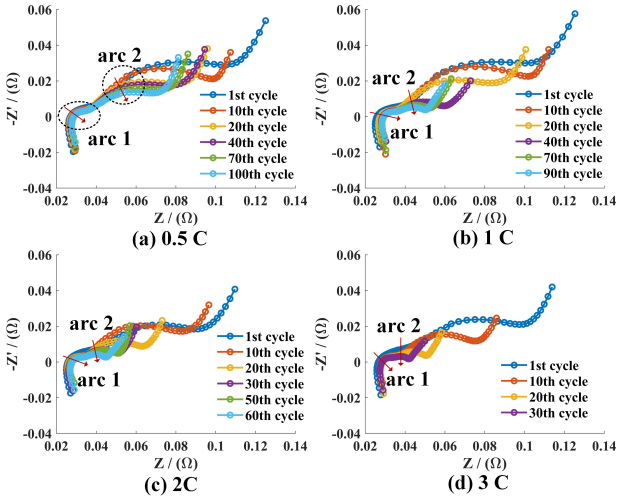

Fig. 4: EIS test results under swaying conditions.

1) EIS test results analysis: From Fig. 4 (a) and (b), as the number of cycles increases, the intersection point with the real axis gradually shifts to the right, and the diameter of the first "arc 1" decreases, representing that, as the performance degradation of LiBs, the ohmic resistance will increase and the SEI film resistance will decrease. Contrary to expectations, the second "arc 2" gradually decreases with aging, presenting swaying facilitates the charge transfer, which is conducive to accelerating the migration of lithium ions between the electrodes and the electrolyte. The possible reason is that swaying makes the active substances in the electrolyte more uniform. This "wetting" effect impacts the polarization reaction, as concluded in Reference [12].

To further investigate the above behaviors, a second-order fractional-order equivalent circuit model (FOECM) with a commercial parameter identification software ZView 3.1 is employed to approximate the measured EIS curves, thereby reflecting the parameter variations of the physical elements. The results are shown in Fig. 5.

From Fig. 5(a), the ohmic resistance R_0 increases significantly with the number of cycles, increasing the CL. The main reasons are as follows: 1) The anode SEI film is damaged by the mechanical stress, which increases irregular pores and reduces porosity in the lithium-ion transport channels, thereby reducing the lithium-ion transport rate; 2) The damage to the electrode material structure can reduce lithium-ion intercalation efficiency. Furthermore, from Fig. 5(b) and (c), both the SEI film resistance R_{sei} and the charge transfer resistance R_{ct} exhibit a decreasing trend. Because electrolyte convection

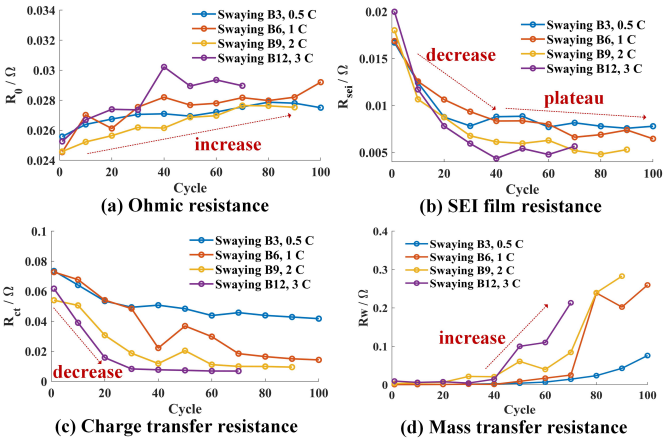

Fig. 5: Physical element parameters under swaying conditions

caused by swaying is enhanced, representing that the "wetting" effect mitigates the impact of activation polarization, which improves the transport efficiency of lithium-ion at the electrode/electrolyte interface. From Fig. 5(d), the increase in mass transfer resistance R_w indicates that the transfer rate of active materials is slowed down due to the increases in LAM, which can decrease the lithium diffusion efficiency.

2) SEM and XRD test results analysis: As shown in Fig. 6(a)-(e), based on the SEM testing, obvious morphological features appear on the surface of the anode at different current rates, including the SEI film growth, deposition of side reaction products, irregular porosity generation, and particle cracking. This indicates that under the long-term influence of swaying stress effects, the degradation of electrode materials is inevitable, and these degradation mechanisms occur concurrently. From Fig. 6 (f), the anode material's crystal structure and composition are analyzed using XRD, i.e., 1) The presence of lithium compounds on the anodes under swaying confirms that lithium-ions react with the active substances in the electrolyte and deposit to form the SEI film. Especially, the formation of inorganic compounds such as LiH, Li_2CO_3, LiF enhances the conductivity of the electrode surface, corroborating the conclusion that the SEI film resistance R_{sei} depicted in Figure 5 (b) decreases with the number of cycle; 2) Compared to the 1 C condition, there is one fewer diffraction peak under the 3 C condition, and the remaining peaks are broader, indicating structural collapse. Additionally, a peak near 60° shifts, suggesting an unstable phase change, which can cause severe damage to the crystal structure.

D. Dominant aging mode analysis of LiBs under swaying

Based on the above analysis, the swaying effects are described as follows: 1) During the early aging stages (0-40 Cycles), ohmic polarization is enhanced, and the "wetting" effect reduces activation polarization and concentration polarization. Swaying stress tends to cause delamination between the active material and the current collector, exacerbating the deposition of reaction products and the SEI layer growth, which reduce the conductivity and increase in R_0, making the rise in CL a

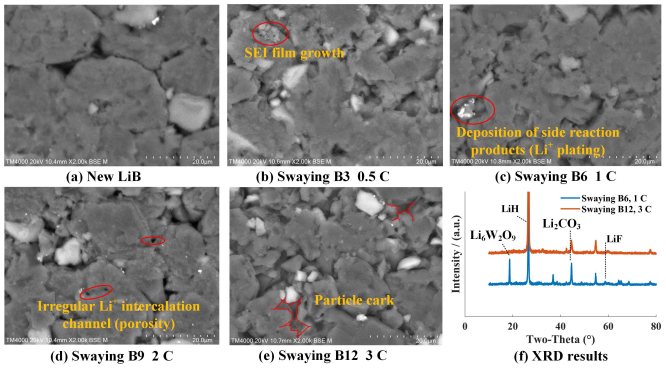

Fig. 6: SEM and XRD test results under swaying conditions.

primary aging factor; 2) During the middle aging stage (40-60 Cycles), the continuous thickening of the SEI film and the accumulation of irreversible physical and chemical structural damage intensify activation polarization and concentration polarization. The degradation rate of R_{sei} and R_{ct} significantly slows down, and R_0 continues to increase. Thus, the CL still remains the dominant aging mode; 3) During the late aging stage (after 60 Cycles), the rate of increase in ohmic impedance R_0 slows down, and the resistance of mass transfer significantly increases and the LAM dominates, representing the particle cracking limit the lithium-ion intercalation and migration, which is more obvious in high current conditions.

III. Physics-informed Degradation Mechanism Modeling under Swaying

A. The integration of physical characteristics under swaying

Based on a clear understanding of the underlying aging mechanisms, the aging mode of LiBs under swaying can be identified. Then, the physical information about EIS impedance obtained from the swaying tests can be utilized to calibrate the essential parameters of numerical simulation models, including: 1) the ohmic resistance R_0 always be employed to correct the terminal voltage variations across different cycles [24]; 2) the SEI film resistance R_{sei} can be used to revise the overpotential and energy loss caused by the SEI layer growth [41]; 3) the charge transfer resistance R_{ct} can be used to correct the interface reaction current density of electrode, i.e., the smaller the R_{ct}, the faster the interfacial reaction rate [42]; 4) Moreover, the mass transfer impedance R_w alone cannot directly identify the mass transfer/diffusion rate following the LiB aging, because the mass transfer process is highly affected by the diffusivity, particle structure, electrolyte concentration, etc.

Therefore, a coupled degradation mechanism should be established to comprehensively reflect the health degradation of LiBs under swaying effects.

B. Coupled degradation mechanisms modeling

Based on an advanced open-source mathematical modeling framework PYBAMM [44], a universal P2D model is used to describe the Li^+ diffusion and migration in the electrode-separator-positive electrode, as shown in the Table. II. Then, as shown in Fig. 7, a coupled degradation mechanism is used to describe the particle-level degradation [45], including: 1) the growth of the SEI layer consumes available lithium ions, solvent molecules, and other active substances, especially the inorganic components produced by the reaction can increase the conductivity and reduce film resistance, 2) the lithium stripping and plating will inevitably form dead lithium and increase LLI, 3) the particle cracking generates additional SEI layer, especially in the extreme case of complete particle detachment, where the binder further exacerbates LAM.

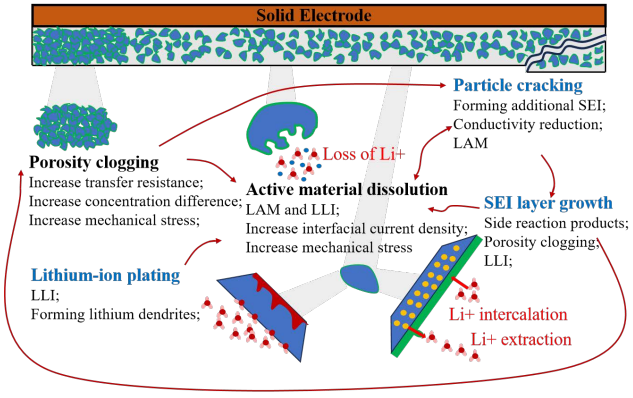

Fig. 7: Coupled degradation mechanism of LiBs.

1) SEI layer growth: The SEI layer may repeatedly fracture and regrow under mechanical stress effects, thereby causing porosity clogging to isolate active regions and restricting the diffusion of solvent molecules. Based on the reference [8], the SEI thickness variation can be formulated by equation (1).

$$\frac{\partial l_{sei}}{\partial t} = -\frac{1}{2} N_{sol} V_{sei} = \frac{c_{sol} D_{sol} V_{sei}}{2 l_{sei}} \tag{1}$$

where l_{sei} is the thickness (m) of SEI layer; V_{sei} is the molar volume of SEI layer (m^3/mol); c_{sol} is the solute concentration (mol/m^2); N_{sol} is the lithium flux density (mol/$m^2\cdot$ s). The porosity is further formulated as $\frac{\partial \varepsilon}{\partial t} = -a_{s,n} \frac{\partial l_{SEI}}{\partial t}$ [46].

The solvent molecule can diffuse through the pore of the SEI layer, and the dynamic diffusivity D_{sol} (m^2/s) is a key parameter that affects the diffusion capability, following Fick's law, which can be formulated by equation (2).

$$\begin{cases} N_{sol} = -D_{sol}(T) \dfrac{\partial c_{sol}}{\partial l}, D_{sol} = 0.5 D_e \epsilon_e^{3/2} \varepsilon \\ c_{sol} = 0 \quad \text{at} \quad l = 0, \\ c_{sol} = c_{sol,0} \quad \text{at} \quad l = l_{sei}, \end{cases} \tag{2}$$

where, D_e and ϵ_e are the inherent diffusion coefficent (m^2/s) and volume fraction of the electrolyte, respectively [47]. $c_{sol,0}$ is the initial solute concentration (mol/m^2).

Since the resistive nature of the SEI layer impedes the interfacial current reactions, resulting in an associated energy loss. According to Ohm's law, which states that the voltage drop is directly proportional to the current density. Therefore, an overpotential η_{sei} (V) can be used to describe the energy loss caused by the SEI layer growth. Without loss of generality,

TABLE II: P2D electrochemical model equations for LiBs [43].

Description	Conservation equations	Boundary conditions
Mass conservation of solid phase	$\frac{\partial c_{s,i}}{\partial t} = \frac{D_{s,i}^{eff}}{r^2}\frac{\partial}{\partial r}(r^2\frac{\partial c_{s,i}}{\partial r})$	$\frac{\partial c_{s,i}}{\partial r}\mid_{r=0}=0,\ D_{s,i}^{eff}\frac{\partial c_{s,i}}{\partial r}\mid_{r=R}=-\frac{I_{app}}{a_{s,i}\epsilon_{s,i}F}=-\frac{j}{F}$
Charge conservation of solid phase	$\frac{\partial}{\partial x}(\sigma^{eff}\frac{\partial \phi_{s,i}}{\partial x})=j$	$\sigma^{eff}\frac{\partial \phi_{s,i}}{\partial x}\mid_{x=0}=\sigma^{eff}\frac{\partial \phi_{s,i}}{\partial x}\mid_{x=L}=I_{app}$
		$\sigma^{eff}\frac{\partial \phi_{s,i}}{\partial x}\mid_{x=L_p}=\sigma^{eff}\frac{\partial \phi_{s,i}}{\partial x}\mid_{x=L-L_n}=0$
Mass conservation of electrolyte phase	$\epsilon_e\frac{\partial c_e}{\partial t}=\frac{\partial}{\partial x}(D_e^{eff}\frac{\partial c_e}{\partial x})+\frac{1-t_+}{F}j$	$\frac{\partial c_e}{\partial x}\mid_{x=0}=\frac{\partial c_e}{\partial x}\mid_{x=L}=0$
Charge conservation of electrolyte phase	$\frac{\partial}{\partial x}(\kappa^{eff}\frac{\partial \phi_e}{\partial x})+\frac{\partial}{\partial x}(\kappa_D^{eff}\frac{\partial lnc_e}{\partial x})+j=0$	$\frac{\partial \phi_e}{\partial x}\mid_{x=0}=\phi_e\mid_{x=L}=0$
Butler-Volmer kinetic	$j=2a_{s,i}i_0 sinh(\frac{0.5F}{R_gT}\eta_{s,i})$	$i_0=k_i\sqrt{c_e(c_s^{max}-c_{s,i}^{surf})c_{s,i}^{surf}},\ k_i=\frac{2R_gT}{FR_{ct}}$

complex factors such as the non-uniformity, multi-layer structure, and temperature variations of the SEI layer are neglected, and a simplified overpotential model is formulated as follows

$$\eta_{sei}=-j\frac{l_{sei}}{\rho_{sei}a_{s,n}}=-jl_{sei}R_{sei} \tag{3}$$

where j is the interface reaction current density of the anode (A/m^2). ρ_{sei} is the ohmic resistivity of the SEI layer (S/m), and $a_{s,n}$ is the specific surface area of anode (m^2). The SEI film resistance R_{eis} is obtained from the test impedance spectroscopy, which can be used to update this model at different cycles.

2) Lithium plating: Li^+ can be stripped and deposited as metallic lithium on the electrode surface, forming the "dead Li", which is formulated as equation (4) [41].

$$\begin{cases}\dfrac{\partial c_{s,n}}{\partial t}=-a_{s,n}N_{s,n}-\underbrace{\gamma(l_{sei})c_{s,n}}_{\text{Dead Li}}\\ LLI=\dfrac{c_{s,n}^{max,0}-c_{s,n}^{max}}{c_{s,n}^{max,0}}\end{cases} \tag{4}$$

where $\gamma(l_{sei})$ is the decay rate of dead lithium (s^{-1}), which is related to the SEI layer growth, i.e., $\gamma(l_{sei})=\gamma_0\frac{l_{sei,0}}{l_{sei}}$, and γ_0 is an initial parameter; $c_{s,n}^{max,0}$ and $c_{s,n}^{max}$ are the initial and current maximum Li^+ concentration (mol/m^3), respectively; $N_{s,n}$ is the Li^+ stripping flux of the anode (mol/m$^2\cdot$ s).

Based on the potential balance, the potential difference describes the variation in potential as lithium-ions de-embed from the solid electrode and migrate into the electrolyte, including both the direct potential difference between the solid and liquid phases and the potential difference across the SEI layer. Therefore, the generated overpotential of the anode lithium-ion plating η_{li} (V) can be formulated by equation (5). This model is based on the assumption of an ideal electrode, i.e., the potential of the solid electrode depends solely on its surface state, and the electrode surface is smooth, and the charge distribution inside the electrode is uniform [41].

$$\eta_{li}=\phi_{s,n}-\phi_e-\eta_{sei} \tag{5}$$

where $\phi_{s,n}$ and ϕ_e are the potential (V) of the anode and electrolyte, respectively.

3) Particle cracking: Affected by mechanical stress effects, frequent volume expansion and contraction of the anode may cause particle crack propagation and material fatigue. Subsequently, new surfaces are exposed to the cracks, thereby accelerating SEI layer growth. In this mode, a verified stress model of the particle can be used to describe the above processes [48], including radial stress σ_r (N), tangential stress σ_t (N), and resultant static stress $\sigma_h=(\sigma_r+2\sigma_t)/3$ (N). Then, the crack length is further formulated by equation (6).

$$\frac{\partial l_{cr}}{\partial N_{s,n}}=\frac{k_{cr}}{t}(\sigma_t b_{cr}\sqrt{\pi l_{cr}})^{mcr},\sigma_t>0 \tag{6}$$

where l_{cr}, t, and b_{cr} are the crack length (m), the operating time (s), and the stress intensity factor, respectively; k_{cr} is the cracking rate of particle, and m_{cr} is a constant. Then, the change rate of the specific surface area $\frac{\partial a_{s,n}}{\partial t}=\frac{2\pi\rho_{cr}w_{cr}}{t_0}\frac{\partial l_{cr}}{\partial N_{s,n}}$ and the change rate of the particle radius $\frac{\partial R}{\partial t}=\frac{V_nR}{3}c_{avg}$ can be further described. Wherein, ρ_{cr} and w_{cr} are the crack number and the crack wide (m), respectively; V_n and c_{avg} are the molar volume (m^3/mol) and the average Li^+ concentration (mol/m^3), respectively.

Then, the additional SEI layer thickness on cracks $l_{sei,cr}$ (m) is formulated by equation (7), which will be feedback into equation (1) and (4) to update the SEI film thickness.

$$\frac{\partial l_{sei,cr}}{\partial t}=\frac{\partial l_{sei}}{\partial t}-\frac{\partial l_{cr}}{\partial t}\frac{l_{sei,cr}(t)-l_{sei,cr}(0)}{l_{cr}} \tag{7}$$

Furthermore, the variations in the volume fraction of the anode and the LAM are formulated by equation (8) [49].

$$\begin{cases}\dfrac{\partial \epsilon_n}{\partial t}=\alpha_1(\dfrac{\sigma_h}{\sigma_{yield}})^{\alpha_2}\\ LAM=(\epsilon_{s,n}^0-\epsilon_{s,n})/\epsilon_{s,n}^0\end{cases} \tag{8}$$

where α_1 is the deacy rate of the volume fraction, and α_2 is a constant; σ_{yield} is the yield strength of the anode; $\epsilon_{n,0}$ is the initial volume fraction.

Finally, the terminal voltage U_{bat}, the SOC SOC_{bat}, and the electrode capacity C_{bat} is calculated by equation (9).

$$\begin{cases}U_{bat}=(\phi_{s,p}+\eta_p)|_{x-L}-(\phi_{s,n}+\eta_n)|_{x-0}-R_0I_{app}\\ SOC_{bat}=c_{s,n}^{surf}/c_{s,n}^{max}=\dfrac{3}{R}\displaystyle\int_0^R c_{s,n}(r)r^2dr\mid_{r=R}/c_{s,n}^{max}\\ C_{bat}=a_{s,n}L\epsilon_{s,n}(c_{s,n}^{max}-c_{s,n}^{min})\end{cases} \tag{9}$$

Based on the above processes, the particle-level degradation behaviors of LiBs can be quantified, thereby effectively capturing the impact of swaying on LiB characteristics.

C. Aging parameter identification

Based on the above model, various parameters should be accurately identified, especially the aging parameters that directly characterize the degradation behaviors of LiBs, including the decay rate of dead lithium γ_0, the cracking rate k_{cr}, the decay rate of the volume fraction α_1, the maxium lithium concentration $c_{s,i}^{max}$, the volume fraction of electrode $\epsilon_{s,i}$ and electrolyte ϵ_e, etc. Drawing on the existing work [50], an optimization problem is formulated to minimize the voltage error between the measurements U_{real} and the model output U_{bat} at different cyclic numbers, as shown in Fig. 8.

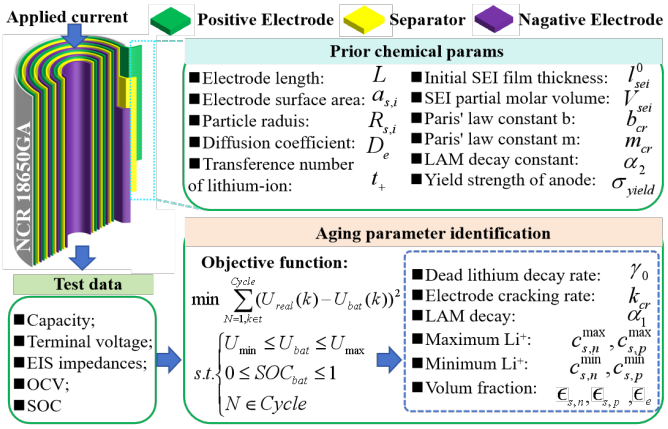

Fig. 8: The parameter identification framework.

The identification is conducted at the N=[1,20,40,60-th] cycles to validate the adaptability of this work under different health levels. A validated particle swarm optimization (PSO) method is used to resolve the optimization problem, and the genetic algorithm (GA) and empirical calibration (EC) methods are used for comparative analysis, with the general mean absolute error (MAE) measuring the accuracy of the results. Note that the knowledge of the EC method is primarily derived from existing studies [47], [48], [51]. As for the PSO method, the swarm size is set to 200, and the function tolerance is set to $1e-6$. Finally, the identification results are shown in Fig. 9 and Table. III.

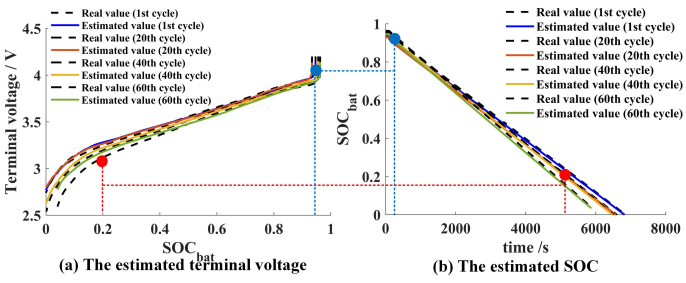

Fig. 9: The identification result of macro parameters.

Generally, the time cost of the PSO method is lower than that of the GA and EC method, which performs better in searching for the global optimum. Although the identification errors of the voltage and SOC increase gradually with the health degradation of LiBs, their absolute value generally meets the requirement, i.e., smaller than 5%. Therefore, the PSO is selected because of the trade-off between computation complexity and accuracy. Finally, the key parameters of NCR 18650GA LiBs are shown in the Table. IV.

TABLE III: The comparsion between different methods.

Cycles	Metrics	PSO	GA	EC
1	Optimization time	**11.35 s**	13.52 s	-
	MAE of voltage	**1.01%**	1.03%	2.81%
	MAE of SOC	0.95%	**0.92%**	3.97%
20	Optimization time	**10.99 s**	12.76 s	-
	MAE of voltage	**1.35%**	1.65%	3.73%
	MAE of SOC	0.93%	0.93%	2.63%
40	Optimization time	**9.86 s**	13.36 s	-
	MAE of voltage	**1.69%**	1.77%	4.72%
	MAE of SOC	**1.26%**	1.32%	5.29%
60	Optimization time	**9.93 s**	14.72 s	-
	MAE of voltage	**3.2%**	3.9%	7.72%
	MAE of SOC	**1.82%**	1.99%	7.33%

TABLE IV: The electrochemical parameters.

Parameters	Value	Units	Source
$R_{s,n}$	5.86e-06	[m]	Ref [48]
$R_{s,p}$	5.22e-06	[m]	Ref [48]
L	0.065	[m]	Ref [48]
$a_{s,i}$	0.00531	[m^2]	Ref [48]
R_0	$[R_0^1, R_0^2, ..., R_0^N]$	[Ω]	EIS testing
R_{sei}	$[R_{sei}^1, R_{sei}^2, ..., R_{sei}^N]$	[Ω]	EIS testing
k_i	$\frac{2R_gT}{FR_{ct}}$	[-]	EIS testing
$l_{sei,0}$	5e-9	[m]	Ref [47]
V_{sei}	9.585e-05	[m]	Ref [47]
t_+	0.363	[-]	Ref [51]
b_{cr}	1.12	[-]	Ref [47]
m_{cr}	2.2	[-]	Ref [47]
α_2	2	[-]	Ref [47]
σ_{yield}	6e7	[-]	Ref [47]
Aging parameters	Value	Units	Source
γ_0	1e-6	[-]	Optimization
k_{cr}	1.9e-20	[-]	Optimization
α_1	8.05e-5	[-]	Optimization
$c_{s,n}^{max,0}$	2.89e4	[mol/m^3]	Optimization
$c_{s,p}^{max,0}$	7.69e4	[mol/m^3]	Optimization
$c_{s,n}^{min,0}$	1.295e4	[mol/m^3]	Optimization
$c_{s,p}^{min,0}$	5.53e4	[mol/m^3]	Optimization
$\epsilon_{s,n}^0$	0.609	[-]	Optimization
$\epsilon_{s,p}^0$	0.322	[-]	Optimization
ϵ_e^0	0.3	[-]	Optimization

Based on the above identified parameters, the electrode capacity losses at different operating conditions are calculated, as shown in Fig. 10, i.e., $C_{loss} = C_{bat}^0 - C_{bat}$. The proposed model that integrates aging parameters across diverse operating conditions closely aligns with the degradation curves observed under both swaying and static conditions. These results verified that the coupled degradation mechanisms can faithfully replicate the actual health degradation of LiBs and mirror their capacity decay trends.

However, there are still some potential degradation factors that the model struggles to capture, leading to deviations in capacity loss at high current rates. For example, the error is 0.034 Ah under swaying conditions and 0.26 Ah under static conditions. Moreover, the large number of PDE equations increases the computational complexity of the model. Therefore, it is necessary to introduce more efficient methods to enhance the model's accuracy and computational efficiency.

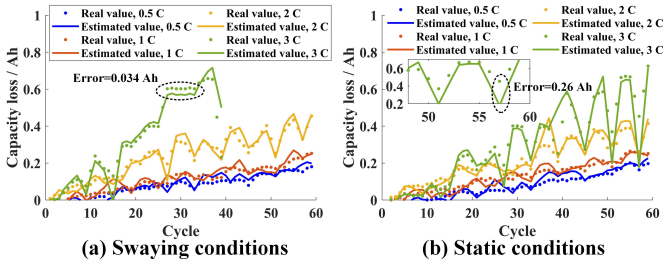

Fig. 10: The electrode capacity loss at different conditions.

IV. Enhanced Physics-Informed Aging Model

In this section, an enhanced PIBM framework that integrates coupled degradation mechanisms is investigated to estimate the health degradation of LiBs from the particle to the cell level, while balancing accuracy and efficiency, as shown in Fig. 11.

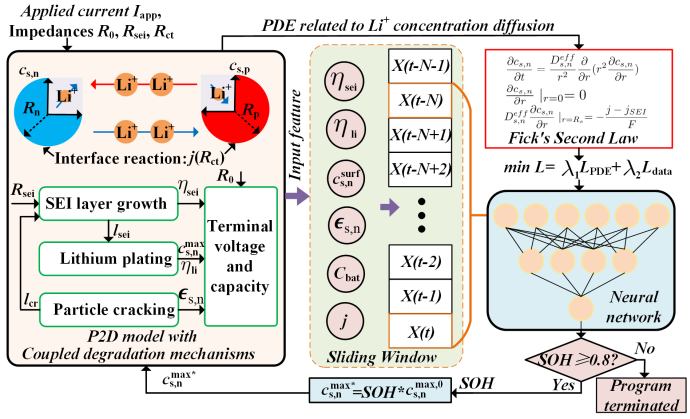

Fig. 11: PIBM with coupled degradation mechanisms.

1) The electrochemical model is used to acquire input features for the data-driven part: Based on the developed P2D model in Section III, the applied current I_{app} collected in real time is used as the input of the modified P2D model to calculate the lithium-ion concentration $c_{s,n}^{surf}$ of the anode surface, the overpotential η_{sei} and η_{li}, the volume fraction of the anode $\epsilon_{s,n}$, the interface reaction current density j, and the electrode capacity C_{bat} in current discharging/charging cycle. These results are stored in the form of a time series in the data log and are extracted through a sliding window sampling method with N-step samples. This method can avoid the high computational cost caused by full data input while retaining the recent state change trend of the LiB.

2) The data-driven part is used to calculate the gradients and minimize the loss function value: Based on the obtained six key electrochemical features, they are utilized as scrolling inputs for the data-driven part to continuously update the neural network. Then, a physical residual related to Fick's second law is incorporated as a component of the loss function, which strictly restrains the physical behaviors. In this mode, a classic neural network such as back-propagation learning machine (BPLM) adheres to the chain rule of forward propagation and backpropagation to calculate the gradients, thereby updating the network's weights and biases. Subsequently, it completes the training until the loss function converges to a predefined minimum value. The SOH in the current charge-discharge cycle can be obtained, and the maximum lithium-ion concentration $c_{s,n}^{max*}$ derived from the SOH is returned to the P2D model to calibrate the aging state of the P2D model for the next charge-discharge cycle.

A. Feature selection

1) Overpotential: Overpotential η_{sei} and η_{li} can reflect the impact of swaying-induced mechanical stress on the SEI layer growth and lithium plating. As shown in Fig. 12 (a1)-(d1), the overpotential increases during charging and then decreases to a negative value during discharging. Because the polarization effect is limited at the beginning of discharge. Meanwhile, the ion transmission resistance is small, and the η_{sei} tends to decrease. Then, under various current conditions, the generated overpotential η_{sei} affected by swaying effects is always higher than that under static conditions. From Fig. 12 (e1), the electrode material structure begins to accumulate damage due to lithium ion deintercalation and other side reactions, leading to a significant increase in η_{sei} as the cycle number increases. From Fig. 12 (a2)-(d2), at low current rates, swaying results in less polarization during lithium plating, bringing a smaller overpotential η_{li}. However, as the discharge rate increases, the overpotential under swaying conditions becomes larger compared to static conditions, since swaying conditions exacerbate the polarization effect. From Fig. 12 (e2), with increasing cycle numbers, the breakdown of the electrode structure leads to reaction inhomogeneity, thereby gradually decreasing the lithium stripping and plating reaction, and the growth of the SEI film is dominant. The above results indicate that swaying intensifies the polarization effect.

2) Other side reaction features: The volume fraction ϵ_n and interfacial current density j can describe the particle cracking effects and electrochemical activity. Additionally, the lithium-ion concentration $c_{s,n}^{surf}$ can be used to describe the non-uniform lithium-ion transport rate affected by mechanical stresses. Moreover, the estimated electrode capacity C_{bat} can be used to supply the assement of the cell health level.

B. Physics-informed task generative model

The nonlinear relationship between input features and outputs is calculated by automatic differentiation within physical constraints. Using the central difference, the discrete physics loss is formulated by the equation (10) and equation (11).

$$L_{PDE} = \frac{1}{N}\sum_{k=1}^{N} \| \underbrace{\frac{\partial c_{s,n}}{\partial t} - \frac{D_{s,n}^{eff}}{r^2}\frac{\partial}{\partial r}(r^2\frac{\partial c_{s,n}}{\partial r})}_{\text{Physics residual based on Fick's second law}} \|^2,$$
$$= \frac{1}{N}\sum_{k=1}^{N} \left\| \Delta c_{s,n}^{t} - \frac{D_{s,n}^{eff}}{r_k^2}\frac{(r_{k+1}^2\Delta c_{s,n}^{r}) - (r_{k-1}^2\Delta c_{s,n}^{r-1})}{2\Delta r} \right\|^2 \quad (10)$$

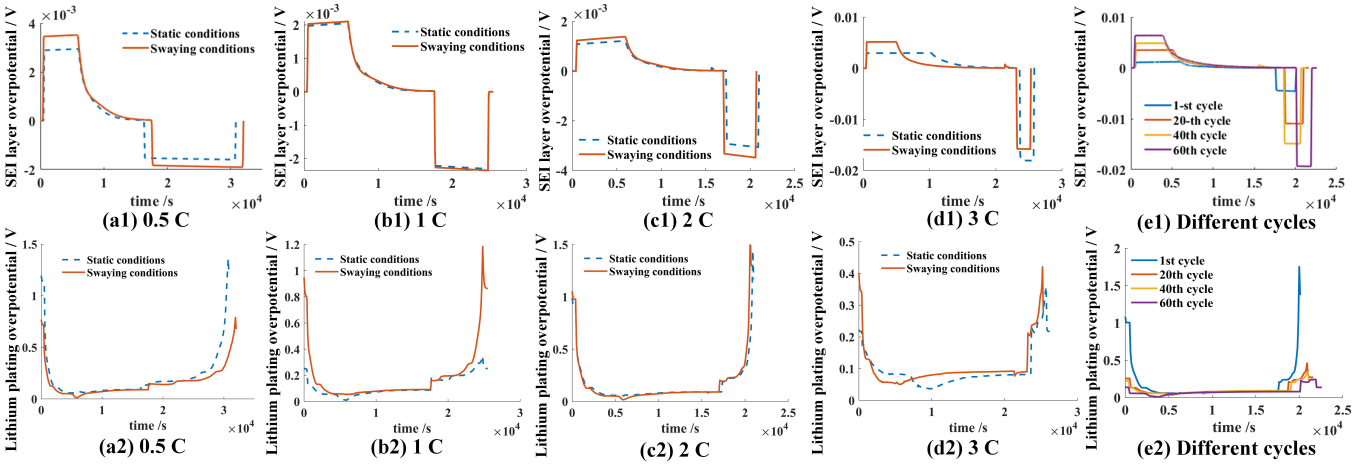

Fig. 12: (a1-d1) SEI layer overpotential at different conditions; (a2-d2) Lithium plating overpotential at different conditions. (e1) SEI layer overpotential under swaying and different cycles. (e2) Lithium overpotential under swaying and different cycles.

$$\begin{cases} c_{s,n} \in [0, c_{s,n}^{max}], \Delta c_{s,n}^{t} = \dfrac{c_{s,n}^{t+\Delta t} - c_{s,n}^{t}}{\Delta t} \\ \Delta c_{s,n}^{r} = \dfrac{c_{s,n}^{r_{k+1}} - c_{s,n}^{r_k}}{\Delta r}, \Delta c_{s,n}^{r-1} = \dfrac{c_{s,n}^{r_k} - c_{s,n}^{r_{k-1}}}{\Delta r} \\ \dfrac{\partial c_{s,n}}{\partial r}\Big|_{r=0} = 0, \quad D_{s,n}^{eff} \dfrac{\partial c_{s,n}}{\partial r}\Big|_{r=R} = -\dfrac{j - j_{sei}}{F} \end{cases} \tag{11}$$

L_{data} is used to formulate consistency between the predicted model output and the test data, as follows:

$$L_{data} = \frac{1}{N}\sum_{k=1}^{N}\{\beta_1 \underbrace{\| \frac{c_{s,n}^{surf}}{c_{s,n}^{max}} - \frac{-\int_{t-N}^{t} I_{app}(k)dt}{3600 C_{real}}) \|^2}_{\text{SOC residual}} + \beta_2 \underbrace{\| SOH - SOH_{real} \|^2}_{\text{SOH residual}}\} + \beta_3 \underbrace{\| U_{cell} - U_{real} \|^2}_{\text{Voltage residual}}\}, \tag{12}$$

where SOH_{real} is the real health state, and U_{real} is the tested terminal voltage under a discharging stage.

Furthermore, the total loss function is formulated as follows:

$$minL = \lambda_p L_{PDE} + \lambda_d L_{data} \tag{13}$$

where $\lambda(\lambda_p = \frac{\partial L}{\partial L_{PDE}}, \lambda_d = \frac{\partial L}{\partial L_d})$ is the global loss weight.

Furthermore, by minimizing the total loss function, the training process is summarized in Algorithm 1.

Finally, the developed PIBM is established in the Python 3.12 and PYBAMM environment equipped with NVIDIA GeForce RTX 2060Ti with 24 GB of memory. The hyperparameter is selected by manual adjustment, as shown in Table V. Then, the first 50% of the data from the Swaying B1, B4, B7, and B12 experimental groups and the Static B3, B6, B9, B11 are used for training, while the remaining 50% is utilized for validation. Moreover, for testing and generalization analysis, we employ data from the Swaying groups B3, B6, B9, and B10, along with the Static groups B1, B4, B8, and B10.

Algorithm 1 Training processes of the proposed PIBM.

Input: The applied current and impedance information $[I_{app}, R_0, R_{sei}, R_{ct}]$
Output: The cell health state, SOH
1: Aging parameter identification.
2: **for** epoch=1,2,$\cdots$ do:
3: Calculating the electrochemical model:
4: $[k_i, \eta_{sei}, \eta_{li}, U_{bat}, SOC_{bat}, C_{bat}] \leftarrow$ Aging mechanisms
5: $[\eta_{sei}, \eta_{li}, c_{s,n}^{surf}, \epsilon_{s,n}, j] \leftarrow$ Obtain features
6: Computing the data-driven model:
7: $[SOH^*] \leftarrow \bigtriangledown_{w,b} L$
8: $L_{PDE}(c_{s,n}^{*}, D_{s,n}^{eff}) \leftarrow$ Compute physcis loss (10)
9: $c_{s,n}^{surf}(c_{s,n}^{*}, R) \leftarrow$ Update the surface concentration
10: $L_{data}(SOH^*) \leftarrow$ Compute data loss (12)
11: $L_{total} \leftarrow$ Back-propagate and update λ (13)
12: $[c_{s,n}^{max}] \leftarrow$ Feedback update the P2D model
13: **end**

TABLE V: The hyperparameter of the data-driven model.

Description	Setting
Number of neurons	[512 256 128 128 3]
Maximum number of iterations	1000
Learning rate	0.001
Training function	Adaptive Moment Estimation(ADM)
Regularization	L2=0.001
Initial weight change	0.07
Training batch size	32

V. Results and Discussion

In this section, the developed physics-informed modeling framework is used to estimate the health degradation of LiBs under swaying. Then, a BPLM without physical processes and a general OLHM are used as the reference to verify the proposed PIBM. The characteristics of these methods are summarized in the Table. VI.

A. Computational complexity analysis of methods

The training and validation processes of different data-driven methods are shown in Fig. 13. The curves represent

TABLE VI: The characteristics of the reference methods.

Methods	Input features	Characteristics
BPLM	• OCV, dV/dQ, dQ/dV, Differential voltage, self-discharging rate.	• Without physical modeling processes.
OLHM	• $\eta_n, c_{s,n}^{surf}, \epsilon_{s,n}, C_{bat}, j.$	• Without integrating the tested physical information and the physical constraints.
PIBM	• $\eta_{sei}, \eta_{li}, c_{s,n}^{surf}, \epsilon_{s,n}, C_{bat}, j.$	• Integrating the tested physical information and the physical constraints.

loss, and the shaded areas represent confidence intervals. Narrower confidence bounds indicate a more stable numerical computation process and better model performance, which provides insights into the model's stability and generalization during training and validation. As for BPLM, due to the absence of detailed electrochemical degradation features, the BPLM exhibits relatively slow convergence, characterized by higher training loss and lower training accuracy, as shown in Fig. 13 (a) and (b). Then, the OLHM can utilize more detailed degradation features to approximate the training object, thereby obtaining less training and validation losses. However, due to the lack of physical constraints related to lithium-ion dynamics, the method exhibits significant oscillations in the validation curve after epoch = 200, as shown in Fig. 13 (c) and (d), easily resulting in the model overfitting. In contrast, the proposed PIBM can achieve the convergence faster and with narrower confidence intervals, indicating better performance stability. Although the validation accuracy curve displays notable oscillations during the early stages of training, the model ultimately achieves satisfactory validation accuracy.

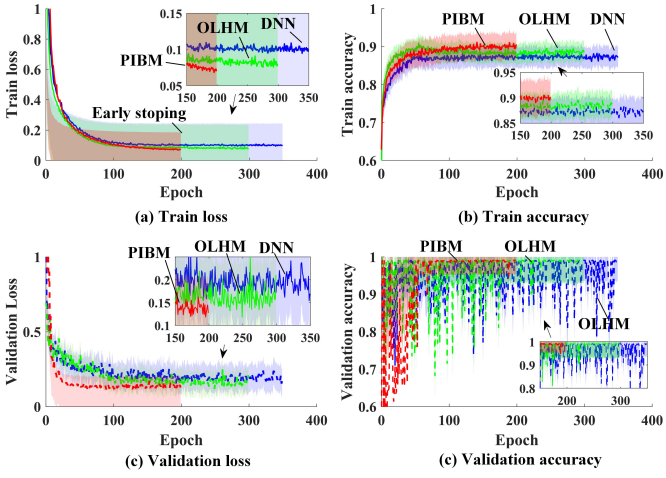

Fig. 13: Training and validation processes.

Furthermore, the calculation complexity of different methods is shown in Fig. 14.

From Fig. 14 (a), the convergence paths of the methods are given, with the proposed PIBM demonstrating a faster gradient descent path. This efficiency is attributed to the use of fully connected layers to replace the complex PDEs associated with the calculation of Li^+ concentration, thereby rapidly approaching the target function value. From Fig. 14 (b), the computational time represents the required solving time for different methods in each cycle. The computational

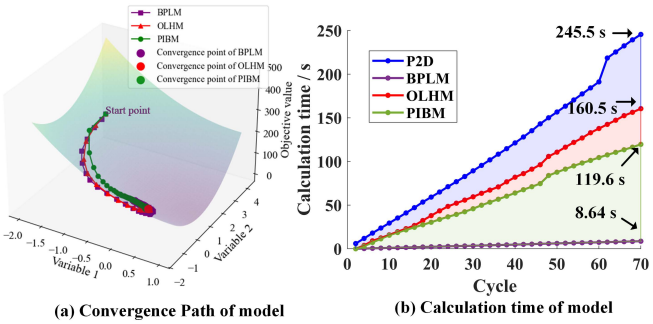

Fig. 14: Calculation complexity of methods.

complexities of the P2D and the BPLM are the highest (245.50 s) and lowest (8.64 s), respectively. The former requires real-time solving of a large number of PDEs, while the latter does not involve any physical processes and can quickly predict the model state using only the pre-trained fully connected layer. Then, the OLHM employs a rolling time window to calculate the electrochemical parameters and uses them as input features of the neural network. This approach avoids additional computational resource consumption of real-time solutions, with the total time required being 160.50 s. Within the proposed PIBM, the PDE related to Li^+ concentration diffusion is replaced by a neural network to reduce the model's complexity, with the final computation time being 119.60 s, and can be reduced by 25.48% compared to OLHM.

B. Estimation effects of health degradation

1) Particle-level analysis of LLI and LAM under swaying: The loss of lithium inventory and active material is calculated based on equations (4) and (8), as shown in Fig. 15.

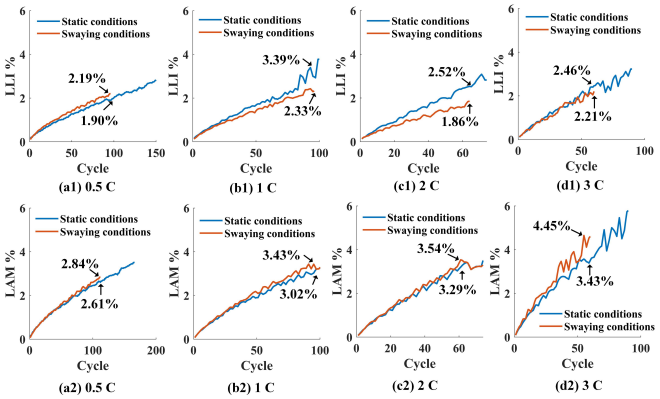

Fig. 15: The LLI and LAM under different conditions.

From Fig. 15 (a1)-(d1), swaying raises LLI by 0.29% compared to static conditions under 0.5 C. This is because electrochemical reactions at the electrode interface are slower at low current rates, making the lithium-ion insertion and extraction processes more sensitive to mechanical stresses. In contrast, under conditions above 1 C, swaying leads to a more uniform distribution of the electrolyte and more complete reactions, resulting in relatively lower LLI compared to static conditions. From Fig. 15 (a2)-(d2), the rate of change in

LAM is faster under swaying than under static conditions due to external mechanical stress on battery materials and structure. With increasing discharge current rates, LAM rises notably. Specifically, it jumps by 1.02% at a 3 C discharge rate compared to static conditions. This indicates that the stress from swaying and high current rates combine to intensify particle structure degradation.

2) Cell-level health estimation under swaying: The estimated SOH of different methods under swaying conditions is shown in Fig. 16. The performance is evaluated using root mean square error (RMSE) and mean absolute percentage error (MAPE), as shown in Fig. 17 and Table. VII.

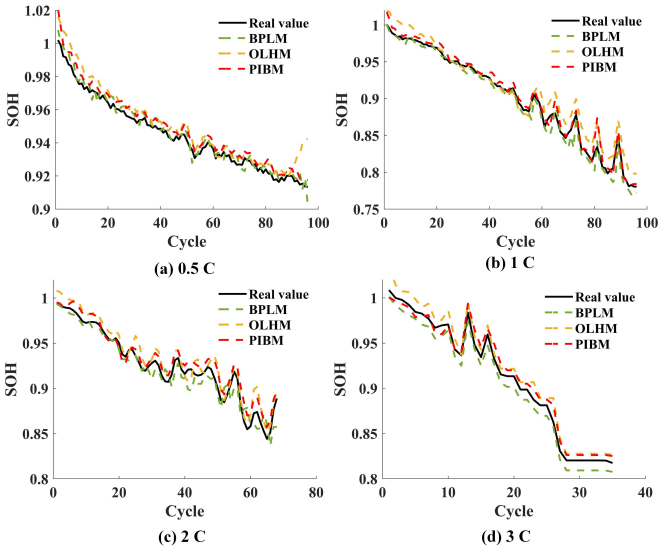

Fig. 16: Estimation effects of SOH under swaying.

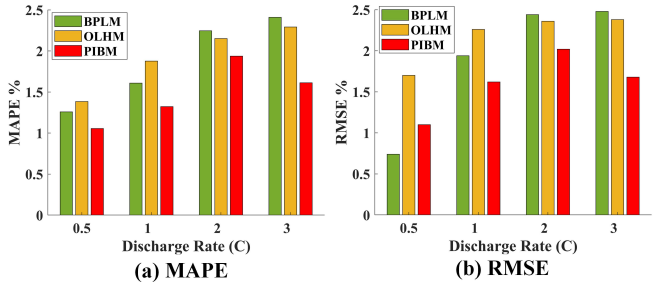

Fig. 17: Estimated errors of different methods.

TABLE VII: Estimated SOH errors under swaying conditions.

Methods	0.5 C	1 C
BPLM	RMSE: **0.74**%, MAPE: **1.26**%	RMSE: 1.94%, MAPE: 1.61%
OLHM	RMSE: 1.70%, MAPE: 1.38%	RMSE: 2.26%, MAPE: 1.88%
PIBM	RMSE: 1.10%, MAPE: 1.06%	RMSE: **1.62**%, MAPE: **1.32**%
Methods	2 C	3 C
BPLM	RMSE: 2.44%, MAPE: 2.25%	RMSE: 2.48%, MAPE: 2.41%
OLHM	RMSE: 2.36%, MAPE: 2.15%	RMSE: 2.38%, MAPE: 2.29%
PIBM	RMSE: **2.02**%, MAPE: **1.94**%	RMSE: **1.68**%, MAPE: **1.61**%

The BPLM offers high computational efficiency and excellent estimation accuracy under 0.5 C, with RMSE at 0.74% and MAPE at 1.26%. However, its performance under higher current rates is less satisfactory. Based on the electrochemical model, the OLHM uses overall degradation characteristics to formulate the health degradation of LiBs. Since these features are mostly extracted from raw data, they may lack the precision of direct measurements like OCV and IC curves, resulting in lower accuracy than the BPLM method. Additionally, the lack of consideration for physical behavior constraints contributes to higher estimation errors. Furthermore, the proposed PIBM can obtain more accurate estimation results under swaying and different current rate conditions. This demonstrates that incorporating coupled degradation mechanisms and physical constraints can effectively improve the model's applicability. Compared with the conventional OLHM method, the PIBM can reduce the SOH estimation error by 28.3% RMSE at most (such as 1C condition).

To further describe the model performance in estimating LiB life trajectories under different initial health states, different SOH estimation results were conducted at different initial cycle counts, and the estimation result is shown in Fig. 18, and the estimation error is shown in Fig. 19. The error represents the difference between the estimated value and the real value.

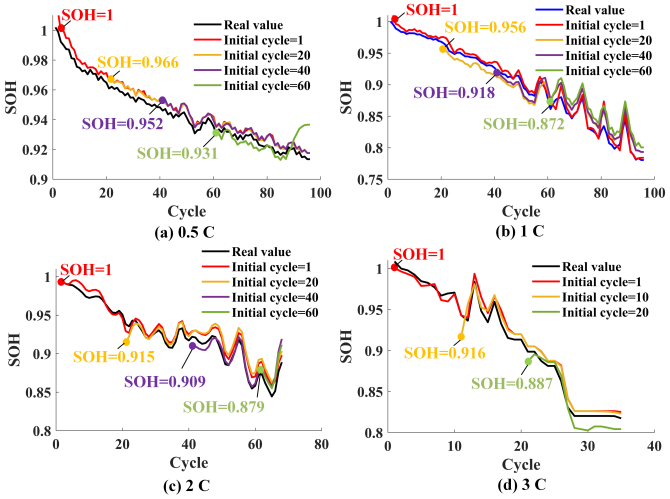

Fig. 18: Estimated results at different initial health states.

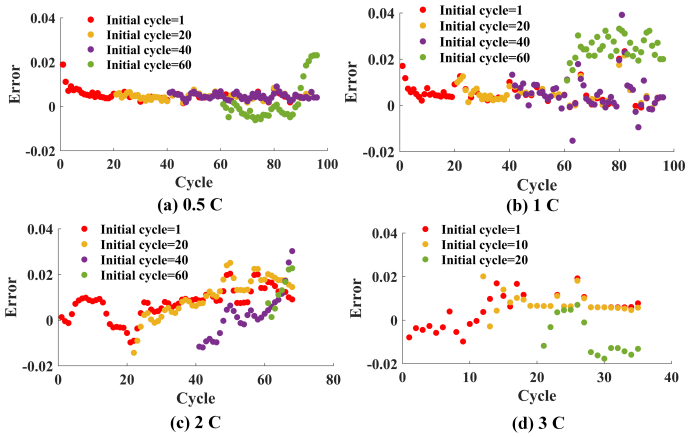

Fig. 19: Estimated errors at different initial health states.

From Fig.18 and Fig. 19, under different initial health states, the proposed model is capable of capturing real health

degradation trajectories. Although the error in health estimation gradually increases with the decrease of initial SOH, the proposed model still obtains a high accuracy in estimating the subsequent health degradation trajectory, with the estimation error not exceeding 4%. The primary reason is that the proposed model scheme consists of two steps, i.e., electrochemical parameter identification and health state estimation. Specifically, 1) the parameter identification part (Fig. 8) can extract aging information from the collected current, voltage, and impedance to identify chemical parameters, thereby approximating the real electrochemical performance of the LiB at different initial health states; 2) the state estimation part (Fig. 11) calculates accurate electrochemical behavior, which serves as the input for the data-driven model, and accurately corrects the estimation result of the health state.

3) Validation of model generalization: To further describe the generalization capability of the proposed PIBM, the estimation results of SOH under static conditions are shown in Fig. 20 and Table. VIII, which is not affected by marine transport swaying conditions. It can be seen that the proposed model can achieve accurate SOH estimation under variable operating conditions. Although the internal stress in the LiBs is relatively low under static conditions, the proposed modeling framework, which adheres to physical laws, can still accurately describe the internal electrochemical behavior, especially the polarization reactions that increase with current rate.

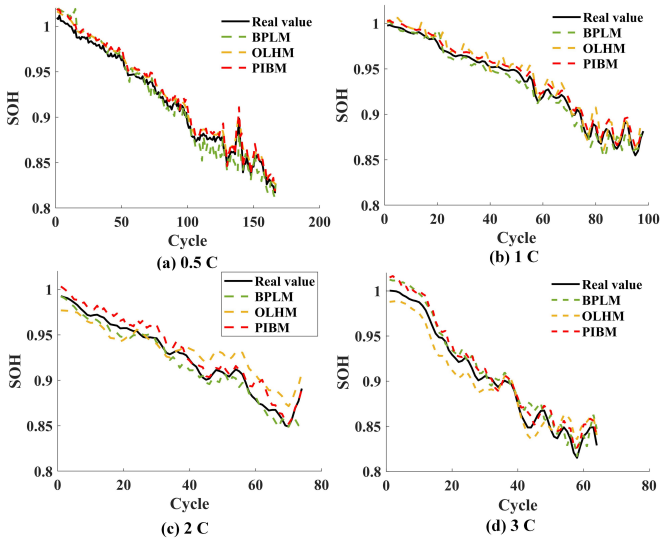

Fig. 20: Estimation effects of SOH under static conditions.

TABLE VIII: Estimated SOH errors under static conditions.

Methods	0.5 C	1 C
BPLM	RMSE: 2.02%, MAPE: 1.78%	RMSE: 1.08%, MAPE: **1.10%**
OLHM	RMSE: **1.44%**, MAPE: **1.52%**	RMSE: 1.50%, MAPE: 1.42%
PIBM	RMSE: 1.60%, MAPE: 1.61%	RMSE: **1.06%**, MAPE: 1.21%
Methods	2 C	3 C
BPLM	RMSE: 2.04%, MAPE: 1.99%	RMSE: 2.16%, MAPE: 2.05%
OLHM	RMSE: 3.24%, MAPE: 3.20%	RMSE: 2.64%, MAPE: 2.66%
PIBM	RMSE: **1.90%**, MAPE: **1.83%**	RMSE: **2.04%**, MAPE: **1.86%**

VI. Conclusion

To efficiently capture the unpredictable health degradation of LiBs under marine transport swaying conditions, a physics-informed battery aging model framework is proposed. The main conclusions are as follows:

1) Based on cyclic LiB testing experiments, this study demonstrates that swaying-induced mechanical stresses accelerate the health degradation of LIBs, including the capacity and voltage decay. The detailed test results demonstrate that the loss of conductivity is a primary aging factor at the early aging stages, and the loss of active material caused by the particle cracking dominates during the late aging stage.
2) The proposed model can quantitatively analyze a particle-level state degradation. The results show that swaying intensify the growth of the SEI layer compared to static conditions, increasing its reaction overpotential. Moreover, the "wetting" effect ensures a more uniform electrolyte distribution and enhanced interface reactions, thus suppressing lithium plating through swaying. However, the mechanical stress caused by swaying damages the particle structure, increasing LAM by 1.02% compared to static conditions.
3) The proposed model can further quantify the cell-level health degradation. Compared with the conventional hybrid data-driven modeling framework, the proposed method reduces computation time by 25.48% and decreases the SOH estimation error by 28.3% at most. Additionally, by integrating the physical behavior constraints, the proposed method still exhibits robust generalization capabilities under static conditions.

References

[1] Persistence Market Research (PMR). Marine lithium-ion battery market. Technical report, tech. rep, 2024.
[2] Pramod Ghimire, Mehdi Zadeh, Shyam Thapa, Jarle Thorstensen, and Eilif Pedersen. Operational efficiency and emissions assessment of ship hybrid power systems with battery; effect of control strategies. *IEEE Transactions on Transportation Electrification*, 10(4):8543–8556, 2024.
[3] Laiqiang Kong, Yingbing Luo, Sidun Fang, Tao Niu, Guanhong Chen, Lijun Yang, and Ruijin Liao. State estimation of lithium-ion battery for shipboard applications: Key challenges and future trends. *Green Energy and Intelligent Transportation*, page 100192, 2024.
[4] Laiqiang Kong, Sidun Fang, Tao Niu, Guanhong Chen, Lijun Yang, and Ruijin Liao. Exploring self-discharge characteristics of lithium-ion batteries corroded by salt spray condition. *Journal of Power Sources*, 630:236182, 2025.
[5] Shuxin Zhang, Zhitao Liu, Yan Xu, and Hongye Su. A physics-informed hybrid multitask learning for lithium-ion battery full-life aging estimation at early lifetime. *IEEE Transactions on Industrial Informatics*, 21(1):415–424, 2025.
[6] Daejeong Kim and Sungwook Lee. Impact of oscillation frequency on hydrodynamic coefficients and its role in ship manoeuvring behaviour. *Ocean Engineering*, 334:121529, 2025.
[7] John Cannarella and Craig B. Arnold. Stress evolution and capacity fade in constrained lithium-ion pouch cells. *Journal of Power Sources*, 245:745–751, 2014.
[8] Anirudh Allam and Simona Onori. Online capacity estimation for lithium-ion battery cells via an electrochemical model-based adaptive interconnected observer. *IEEE Transactions on Control Systems Technology*, 29(4):1636–1651, 2021.
[9] Taylor R. Garrick, Xinyu Huang, Venkat Srinivasan, and John W. Weidner. Modeling volume change in dual insertion electrodes. *Journal of The Electrochemical Society*, 164:E3552, 2017.

[10] Zhi Wang, Qingjie Zhao, Xianyu Yu, Weiguang An, and Bobo Shi. Impacts of vibration and cycling on electrochemical characteristics of batteries. *Journal of Power Sources*, 601:234274, 2024.

[11] Wenhua Li, Yangyang Wang, Fangxu Shao, and Mingze He. Study on the capacity degradation mechanism and capacity predication of lithium-ion battery under different vibration conditions in six degrees-of-freedom. *Journal of Electrochemical Energy Conversion and Storage*, 20(2):1–36, 2022.

[12] James Michael Hooper, James Marco, Gael Henri Chouchelamane, Julie Sylvie Chevalier, and Darren Williams. Multi-axis vibration durability testing of lithium ion 18650 nca cylindrical cells. *Journal of Energy Storage*, 15:103–123, 2018.

[13] Zhongkai Zhou, Yan Li, Qing-Guo Wang, and Jinpeng Yu. Health indicators identification of lithium-ion battery from electrochemical impedance spectroscopy using geometric analysis. *IEEE Transactions on Instrumentation and Measurement*, 72:1–9, 2023.

[14] Chengqi She, Lei Zhang, Zhenpo Wang, Fengchun Sun, Peng Liu, and Chunbao Song. Battery state-of-health estimation based on incremental capacity analysis method: Synthesizing from cell-level test to real-world application. *IEEE Journal of Emerging and Selected Topics in Power Electronics*, 11(1):214–223, 2023.

[15] Zhongrui Cui, Naxin Cui, Changlong Li, Jianbo Lu, and Chenghui Zhang. Online identification and reconstruction of open-circuit voltage for capacity and electrode aging estimation of lithium-ion batteries. *IEEE Transactions on Industrial Electronics*, 70(5):4716–4726, 2023.

[16] Xinhong Feng, Yongzhi Zhang, Rui Xiong, and Aihua Tang. Estimating battery state of health with 10-min relaxation voltage across various charging states of charge. *iEnergy*, 2(4):308–313, 2023.

[17] Fu Wan, Yupeng Lin, Da Yang, Shufan Li, Ruiqi Liu, Lei Zhu, Wenwei Yin, and Weigen Chen. Prediction of state-of-health and remaining useful life for lithium-ion batteries using short-term relaxation voltage. *Journal of Energy Storage*, 129:117397, 2025.

[18] Gaige Chen, Chenglong Wang, Yahong Yang, Xiaoshen Zhang, Wei Deng, and Jinsong Liu. Online condition monitoring and state of health estimation method for lithium-ion batteries based on time-ratio features. *Sustainable Energy Technologies and Assessments*, 79:104364, 2025.

[19] Teng Wang, Yuhao Zhu, Zhen Zhang, Fangyuan Bi, Luoran Sun, Taehyuck Kim, and Yunlong Shang. A soh estimation method within micro-voltage interval based on ica peak distribution for lithium-ion batteries. *IEEE Transactions on Transportation Electrification*, pages 1–1, 2025.

[20] Tianyi Li, Dazhi Wang, Yupeng Zhang, and Tianhao Gong. Application of time domain and frequency domain feature fusion and parseval-bilstm for state of health estimation of lithium-ion batteries. *Journal of Power Sources*, 653:237776, 2025.

[21] Jingqi Gao, Ruitian He, Peng Wu, and Kai H. Luo. Unravelling multi-layered structure of native sei on lithium metal electrode and various electrolytes using reactive molecular dynamics. *Journal of Energy Storage*, 106:114919, 2025.

[22] Yun Wang, Qian Zhou, Fan Zhang, and Runmin Zou. Enhancing state of health estimation of lithium-ion batteries through strategic feature analysis. *IEEE Transactions on Transportation Electrification*, pages 1–1, 2025.

[23] Jonas Keil and Andreas Jossen. Electrochemical modeling of linear and nonlinear aging of lithium-ion cells. *Journal of The Electrochemical Society*, 167:110535, 2020.

[24] Yingbing Luo, Sidun Fang, Laiqiang Kong, Tao Niu, and Ruijin Liao. Dynamic power management of shipboard hybrid energy storage system under uncertain navigation conditions. *IEEE Transactions on Transportation Electrification*, 10(2):3138–3152, 2024.

[25] Jianwen Meng, Meiling Yue, and Demba Diallo. A degradation empirical-model-free battery end-of-life prediction framework based on gaussian process regression and kalman filter. *IEEE Transactions on Transportation Electrification*, 9(4):4898–4908, 2023.

[26] Valentina Bianchi, Mattia Stighezza, Andrea Toscani, Giovanni Chiorboli, and Ilaria De Munari. An improved method based on support vector regression with application independent training for state of charge estimation. *IEEE Transactions on Instrumentation and Measurement*, 72:1–11, 2023.

[27] Mina Naguib, Phillip Kollmeyer, and Ali Emadi. Application of deep neural networks for lithium-ion battery surface temperature estimation under driving and fast charge conditions. *IEEE Transactions on Transportation Electrification*, 9(1):1153–1165, 2023.

[28] Han Zhang, Yuqi Li, Shun Zheng, Ziheng Lu, Xiaofan Gui, Wei Xu, and Jiang Bian. Battery lifetime prediction across diverse ageing conditions with inter-cell deep learning. *Nature Machine Intelligence*, 15:1–12, 205.

[29] Laiqiang Kong, Sidun Fang, Tao Niu, Guanhong Chen, Lijun Yang, and Ruijin Liao. Fast state of charge estimation for lithium-ion battery based on electrochemical impedance spectroscopy frequency feature extraction. *IEEE Transactions on Industry Applications*, pages 1–11, 2023.

[30] Chuanping Lin, Jun Xu, Jiayang Hou, Ying Liang, and Xuesong Mei. Ensemble method with heterogeneous models for battery state-of-health estimation. *IEEE Transactions on Industrial Informatics*, 19(10):10160–10169, 2023.

[31] Renato G. Nascimento, Felipe A. C. Viana, Matteo Corbetta, and Chetan S. Kulkarni. A framework for li-ion battery prognosis based on hybrid bayesian physics-informed neural networks. *Scientific Reports*, 13:1–12, 2023.

[32] Pengfei Wen, Zhi-Sheng Ye, Yong Li, Shaowei Chen, Pu Xie, and Shuai Zhao. Physics-informed neural networks for prognostics and health management of lithium-ion batteries. *IEEE Transactions on Intelligent Vehicles*, 9(1):2276–2289, 2024.

[33] Weihan Li, Jiawei Zhang, Florian Ringbeck, Dominik Jöst, Lei Zhang, Zhongbao Wei, and Dirk Uwe Sauer. Physics-informed neural networks for electrode-level state estimation in lithium-ion batteries. *Journal of Power Sources*, 491:229580, 2021.

[34] Yanan Wang, Xuebing Han, Dongxu Guo, Languang Lu, Yangquan Chen, and Minggao Ouyang. Physics-informed recurrent neural network with fractional-order gradients for state-of-charge estimation of lithium-ion battery. *IEEE Journal of Radio Frequency Identification*, 6:968–971, 2022.

[35] Bing-Chuan Wang, Zhen-Dong Ji, Yong Wang, Han-Xiong Li, and Zhongmei Li. A physics-informed composite network for modeling of electrochemical process of large-scale lithium-ion batteries. *IEEE Transactions on Industrial Informatics*, 21(1):287–296, 2025.

[36] China Classification Society. Guidelines for type approval testing of electrical and electronic products. Technical report, tech. rep, 2015.

[37] Laiqiang Kong, Yingbing Luo, Sidun Fang, Tao Niu, Guanhong Chen, Lijun Yang, and Ruijin Liao. Electrochemical model based soc-soh estimation of lithium-ion batteries under shipboard swaying conditions. *Journal of Energy Storage*, 124, 2025. Cited by: 0.

[38] Yingbing Luo, Laiqiang Kong, Sidun Fang, Tao Niu, Guanhong Chen, Ailong Fan, and Ruijin Liao. Health-aware energy storage system management considering state coupling characteristics for navigation in restricted waters. *IEEE Transactions on Transportation Electrification*, 10(4):7741–7757, 2024.

[39] Gaige Chen, Siqi Zhong, Yahong Yang, Xiaoshen Zhang, Wei Deng, and Jinsong Liu. A lithium-ion battery health state assessment and remaining useful life prediction method based on multi slope features. *Journal of Energy Storage*, 130:117324, 2025.

[40] Tianyi Li, Dazhi Wang, Yupeng Zhang, and Tianhao Gong. Application of time domain and frequency domain feature fusion and parseval-bilstm for state of health estimation of lithium-ion batteries. *Journal of Power Sources*, 653:237776, 2025.

[41] Simon E. J. O'Kane, Weilong Ai, Ganesh Madabattula, Diego Alonso-Álvarez, Robert Timms, Valentin Sulzer, Jacqueline Sophie Edge, Billy Wu, Gregory James Offer, and Monica Marinescu. Lithium-ion battery degradation: how to model it. *Physical chemistry chemical physics : PCCP*, 2021.

[42] Qunming Zhang, Cheng-Geng Huang, He Li, Guodong Feng, and Weiwen Peng. Electrochemical impedance spectroscopy based state-of-health estimation for lithium-ion battery considering temperature and state-of-charge effect. *IEEE Transactions on Transportation Electrification*, 8(4):4633–4645, 2022.

[43] Ali Jokar, Barzin Rajabloo, Martin Désilets, and Marcel Lacroix. Review of simplified pseudo-two-dimensional models of lithium-ion batteries. *Journal of Power Sources*, 327:44–55, 2016.

[44] Valentin Sulzer, Scott G. Marquis, Robert Timms, Martin Robinson, and S. Jon Chapman. Python Battery Mathematical Modelling (PyBaMM). *Journal of Open Research Software*, 9(1):14, 2021.

[45] Zhi Wang, Qingjie Zhao, Shaojia Wang, Yuchen Song, Bobo Shi, and Junjiang He. Aging and post-aging thermal safety of lithium-ion batteries under complex operating conditions: A comprehensive review. *Journal of Power Sources*, 623:235453, 2024.

[46] Xiao-Guang Yang, Yongjun Leng, Guangsheng Zhang, Shanhai Ge, and Chao-Yang Wang. Modeling of lithium plating induced aging of lithium-ion batteries: Transition from linear to nonlinear aging. *Journal of Power Sources*, 360:28–40, 2017.

[47] Chen ChangHui, Brosa Planella Ferran, Dominika Gastol Kieran, ORegan, Widanage W. Dhammika, and Kendrick Emma. Development of experimental techniques for parameterization of multi-scale lithium-ion

battery models. *Journal of The Electrochemical Society*, 167:080534, 2020.

[48] Simon E. J. O'Kane, Ian D. Campbell, Mohamed W. J. Marzook, Gregory J. Offer, and Monica Marinescu. Physical origin of the differential voltage minimum associated with lithium plating in li-ion batteries. *Journal of The Electrochemical Society*, 167:090540, 2020.

[49] Jorn M. Reniers, Grietus Mulder, and David A. Howey. Review and performance comparison of mechanical-chemical degradation models for lithium-ion batteries. *Journal of The Electrochemical Society*, 166:A3189, 2019.

[50] Yuxuan Gu, Jianxiao Wang, Yuanbo Chen, Kedi Zheng, Zhongwei Deng, and Qixin Chen. Electrochemical parameter identification for lithium-ion battery sources in self-sustained transportation energy systems. *IEEE Transactions on Industry Applications*, 60(1):1240–1254, 2024.

[51] Boyang Liu, Xiaopeng Tang, and Furong Gao. Joint estimation of battery state-of-charge and state-of-health based on a simplified pseudo-two-dimensional model. *Electrochimica Acta*, 344:136098, 2020.